STRUCTURAL SCIENCE
CRYSTAL ENGINEERING
MATERIALS

ISSN: 2052-5206
journals.iucr.org/b

Incommensurately modulated structures of the $M_{1/8}Pr_{5/8}MoO_4$ (M = Li, Na, K) scheelites

Vladimir A. Morozov, Dina V. Deyneko, Darya G. Filatova, Alexei A. Belik, Olga M. Basovich, Elena G. Khaikina and Bogdan I. Lazoryak

Acta Cryst. (2026). B**82**, 120–130

Acta Cryst B STRUCTURAL SCIENCE CRYSTAL ENGINEERING MATERIALS

ISSN 2052-5206

Incommensurately modulated structures of the $M_{1/8}Pr_{5/8}MoO_4$ (M = Li, Na, K) scheelites

Vladimir A. Morozov,[a]* Dina V. Deyneko,[a] Darya G. Filatova,[a] Alexei A. Belik,[b] Olga M. Basovich,[c] Elena G. Khaikina[c] and Bogdan I. Lazoryak[a]

[a]Chemistry Department, Moscow State University, 119991, Russian Federation, [b]Research Center for Materials Nanoarchitectonics (MANA), National Institute for Materials Science (NIMS), Namiki 1-1, Tsukuba, Ibaraki, 305-0044, Japan, and [c]Baikal Institute of Nature Management, Siberian Branch, Russian Academy of Science, Ulan-Ude, 670047, Russian Federation. *Correspondence e-mail: morozov111vla@mail.ru

Received 7 November 2025
Accepted 14 January 2026

Edited by T. B. Bekker, Siberian Branch of Russian Academy of Science, Russian Federation

This article is part of a special issue on current research in crystal growth and related characterization

Keywords: incommensurate modulation; crystal structure; scheelite; synchrotron powder X-ray diffraction data; ordering.

B-IncStrDB reference: L8zZeSPwZg1

Supporting information: this article has supporting information at journals.iucr.org/b

The effect of cation substitutions in the scheelite-type framework is investigated to understand the ordering of M^+/Pr^{3+} cations and vacancies in the structure. The cation deficient $M_{1/8}Pr_{5/8}\square_{1/4}MoO_4$ (M = Li, Na, K) phases were synthesized using solid state reactions. The K:Pr ratio in the $K_{1/8}Pr_{5/8}MoO_4$ sample was determined by inductively coupled plasma mass spectroscopy, inductively coupled plasma optical emission spectrometry and total reflection X-ray fluorescence spectroscopy. The local element distributions in $K_{1/8}Pr_{5/8}\square_{1/4}MoO_4$ were determined by energy-dispersive X-ray spectrometry. The incommensurately modulated crystal structures of the scheelite-based $M_{1/8}Pr_{5/8}MoO_4$ (M = Li, Na, K) phases were refined from synchrotron powder X-ray diffraction data. The analysis revealed that cation ordering in the $M_{1/8}Pr_{5/8}MoO_4$ (M = Li, Na) structures is incomplete and is more accurately described by continuous, rather than discontinuous (step-like), occupational modulation functions. The occupancy modulation waves for Li/Na and Pr atoms demonstrate an antiphase relation. Compared with M = Li, Na, the order of K and Pr cations in the A position in the $K_{1/8}Pr_{5/8}MoO_4$ structure is best approximated by crenel functions. Refining the coordinates and lengths of three atomic domains yields the composition of $K_{0.145}Pr_{0.618}MoO_4$. In all cases, the modulation arises from ordering of M/Pr cations and cation vacancies at the A-sublattice of the parent scheelite ABO_4 structure. The distortion of PrO_8 and MO_8 polyhedra is practically independent of the radius of the M^+ cations. The refinements of the $M_{1/8}Pr_{5/8}MoO_4$ (M = Li, Na, K) structures reveal that MoO_4^{2-} tetrahedra in these scheelite-type compounds demonstrate a flexible geometry. Both Mo—O bond distances and O—Mo—O bond angles vary significantly with changing the population of the A site by cations with different sizes.

1. Introduction

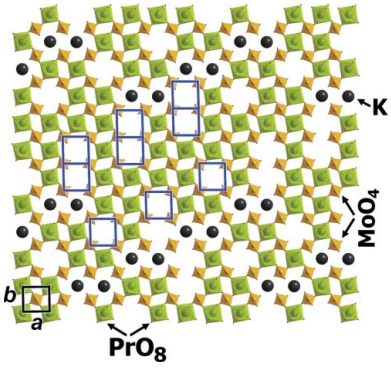

Scheelite related compounds (SRC) with a general formula $(A',A'')_n[(B',B'')O_4]_m$ (A', A'' = Ag, alkali, alkali-earth or rare-earth elements; B', B'' = W, Mo) are a family of inorganic materials that have attracted widespread attention due to their excellent thermal stability, hydrolysis resistance, long lifespan, and low cost. Additionally, they can accommodate various rare earth (RE) activators to achieve effective luminescence. SRC have been widely studied and applied in phosphor converted WLED (white-light-emitting diodes), solid-state lasers, fingerprint detection, environmental lighting, medical treatment, and optical thermometers (Bin *et al.*, 2019; Wu *et al.*, 2021; Lu *et al.*, 2018; Singh *et al.*, 2023; Morozov *et al.*, 2023; Huang *et al.*, 2004; Huang *et al.*, 2018; Zhao *et al.*, 2013; Pusdekar *et al.*, 2025; Meert *et al.*, 2014; Morozov *et al.*, 2018; Zhao *et al.*, 2021; Zhang *et al.*, 2024) *etc.*

The scheelite-type ABO_4 structure consists of columns of vertex sharing AO_8 polyhedra and BO_4 tetrahedra running along the c axis and forming a 3D framework. $CaWO_4$ is the aristotype of this family and has tetragonal symmetry with space group $I4_1/a$. The scheelite-type structures may have lower symmetries, depending on the nature of the A and B cations or the presence of ordered vacancies. The creation of a cation vacancy (□) in the scheelite-type framework and ordering of the A cations and vacancies offers a new parameter for monitoring structure and properties of SRC. The A cations and vacancies can order, frequently forming incommensurately modulated structures (Abakumov *et al.*, 2014; Arakcheeva *et al.*, 2012; Batuk *et al.*, 2017; Morozov *et al.*, 2012; Morozov *et al.*, 2013; Morozov *et al.*, 2017; Morozov *et al.*, 2018; Morozov *et al.*, 2023).

The cationic vacancies formation and the cationic and anionic substitutions in SRC lead to the formation of (3+1)D incommensurate modulated structures, which require a (3+n)D approach. For example, replacing the smaller Gd^{3+} with the larger Eu^{3+} at the A-sublattice in $CaGd_{2(1-x)}Eu_{2x}(MoO_4)_{4(1-y)}(WO_4)_{4y}$ does not affect the nature of the incommensurate modulation. However, increasing replacement of W^{6+} by Mo^{6+} switches the modulation from (3+1)D to (3+2)D regime (Abakumov *et al.*, 2014; Morozov *et al.*, 2013). At low vacancy concentration (<15%) (Arakcheeva *et al.*, 2012; Batuk *et al.*, 2017), cations and cation vacancies are randomly distributed in the structure, and the materials preserve the $I4_1/a$ symmetry of the parent scheelite structure. The structure with 20% vacancies has a (3+2)D tetragonal symmetry (Batuk *et al.*, 2017). Further increasing the cation vacancies from 20% to 25% in $Ca_{0.85-1.5x}Gd_xEu_{0.1}\square_{0.05+0.5x}WO_4$ (Batuk *et al.*, 2017) and from <15% to 17% in $Na_xEu^{3+}{}_{(2-x)/3}MoO_4$ (Arakcheeva *et al.*, 2012), the (3+2)D incommensurately modulated structure undergoes a monoclinic distortion, forming the (3+1)D structure.

In this contribution, we provide the structure refinement for (3+1)D-modulated monoclinic $M_{1/8}Pr_{5/8}\square_{1/4}MoO_4$ (M = Li, Na, K) using synchrotron powder X-ray diffraction and reveal an influence of cationic composition on ordering of M^+/Pr^{3+} cations and vacancies.

2. Experimental

2.1. Materials and sample preparation

$M_{1/8}Pr_{5/8}\square_{1/4}MoO_4$ (M = Li, Na, K) samples were synthesized using solid state reactions from a stoichiometric mixture of M_2MoO_4 (M = Li, Na, K) and $Pr_2(MoO_4)_3$ at 773–1073 K for 70 h in air, followed by quenching from 1073 K to room temperature (T_R). M_2MoO_4 (M = Li, Na, K) samples were prepared using solid state reactions from stoichiometric amounts of M_2CO_3 (99.99%) and MoO_3 (99.99%) at 673–823 K for 60 h. The $Pr_2(MoO_4)_3$ precursor was synthesized using a solid state reaction from Pr_6O_{11} (99.99%) and MoO_3 at 823 K for 10 h, followed by annealing at 1123 K for 80 h. Powder X-ray diffraction (PXRD) patterns of $Pr_2(MoO_4)_3$ matched the $Pr_2(MoO_4)_3$ XRD patterns reported by Logvinovich *et al.* (2010) and did not contain reflections of any foreign phases.

2.2. Characterization

K:Pr ratio for the bulk $K_{1/8}Pr_{5/8}\square_{1/4}MoO_4$ sample was determined: (1) by inductively coupled plasma mass spectrometry (ICP-MS) using a quadrupole Agilent 7500C mass spectrometer (Agilent Technologies, Japan) controlled via the PC software *ChemStation* (version G1834B) package (Agilent Technologies); (2) by inductively coupled plasma optical emission spectroscopy (ICP-OES) using an Agilent 5800 VDV ICP-OES spectrometer (Agilent Technologies, USA); (3) by total reflection X-ray fluorescence spectroscopy (TXRF) using a S2 Picofox spectrometer (Bruker Nano GmbH, Germany) with Mo $K\alpha$ radiation.

The ICP-MS, ICP-OES and TXRF results were obtained by the external standard method using single element (K and Pr) standard solutions (High-Purity Standards, USA). Three samples weighing between 6 and 15 mg were analyzed. A mixture of concentrated nitric and hydrochloric acids (aqua regia) and deionized water (18.2 mQ cm^{-1}) was used for solution preparation. All samples were weighed in a vial and dissolved by aqua regia (1:1). After sample dissolution, the obtained solution was adjusted to a volume of 2 ml with deionized water. Further, the stock solution was diluted 1000-fold for ICP-MS and tenfold for ICP-OES and TXRF measurements in a 10 ml vial using a manual sampler. K $K_{1,2}$ (3.314 keV), Pr L_1 (5.035 keV)$_L$ and Ga $K_{1,2}$ (9.251 keV) lines in the TXRF spectra were used for the element composition study.

A Jeol JSM-6490LV scanning electron microscope (SEM) equipped with an EDX spectrometer INCA X-Sight (Oxford Instruments) was used for SEM observations of $K_{1/8}Pr_{5/8}\square_{1/4}MoO_4$. Samples were coated with a thin layer of carbon for SEM examinations. K_K, Pr_L, and Mo_L lines in the SEM-EDX spectra were used for the element composition study. The oxygen content was not quantified by EDX.

Powder X-ray diffraction patterns of $M_{1/8}Pr_{5/8}\square_{1/4}MoO_4$ (M = Li, Na, K) were collected on a SIEMENS D500 diffractometer equipped with a primary SiO_2 monochromator (Cu $K_{\alpha1}$ radiation, λ = 1.5406 Å, Bragg–Brentano geometry) and a position sensitive detector (BRAUN). PXRD data were collected at T_R in the 7°–140° 2θ range with steps of 0.02°. To determine the unit-cell parameters, the PXRD data were refined by Le Bail decomposition (Le Bail *et al.*, 1988) using the *JANA2006* software (Petříček *et al.*, 2014).

Synchrotron powder X-ray diffraction data for $M_{1/8}Pr_{5/8}\square_{1/4}MoO_4$ (M = Li, Na, K) were measured in a large Debye–Scherrer camera at the BL15XU beamline of SPring-8 (λ = 0.5008 Å) (Tanaka *et al.*, 2008; Tanaka *et al.*, 2013) between 0.1° and 40.52° with a step of 0.0025° in 2θ. The sample was packed into a Lindemann glass capillary (inner diameter 0.1 mm), which was rotated during the measurement. Details of experiments and characteristics of the final structure refinements are listed in Table 1. The Rietveld analysis of

Table 1
Crystal data, data collection and refinement of $M_{1/8}Pr_{5/8}MoO_4$ (M = Li, Na, K).

	Li scheelite	Na scheelite	K scheelite
Crystal data			
Chemical formula	$Li_{0.125}Pr_{0.625}\square_{1/4}MoO_4$	$Na_{0.125}Pr_{0.625}\square_{1/4}MoO_4$	$K_{0.145}Pr_{0.618}\square_{0.237}MoO_4$
M_r	246.5	250.9	252.7
Crystal system, space group		Monoclinic, $I2/b(\alpha\beta0)00$	
Temperature (K)		293	
a, b, c (Å)	5.30263 (1), 5.29792 (1), 11.75179 (2)	5.30752 (3), 5.30900 (3), 11.75478 (3)	5.31857 (1), 5.33959 (1), 11.87729 (3)
γ (°)	90.0184 (4)	90.0084 (9)	90.0509 (2)
V (Å^3)	330.14 (1)	331.22 (1)	337.30 (1)
Wave vectors	$\mathbf{q}$ = 0.568641$\mathbf{a}^*$ + 0.835383$\mathbf{b}^*$	$\mathbf{q}$ = 0.578340$\mathbf{a}^*$ + 0.837694$\mathbf{b}^*$	$\mathbf{q}$ = 0.566419$\mathbf{a}^*$ + 0.836554$\mathbf{b}^*$
Z	4	4	4
D_{calc} (g cm^{-3}	4.959	5.031	4.976
Colour		Light green	
Data collection			
Diffractometer		BL15XU beamline of SPring-8	
Radiation type, λ (Å)	Synchrotron, 0.5008	Synchrotron, 0.5008	Synchrotron, 0.5008
2θ values (°)	$2\theta_{min}$ = 3.148, $2\theta_{max}$ = 45.518, $2\theta_{step}$ = 0.0025	$2\theta_{min}$ = 2.395, $2\theta_{max}$ = 45.518, $2\theta_{step}$ = 0.003	$2\theta_{min}$ = 2.69, $2\theta_{max}$ = 42.818, $2\theta_{step}$ = 0.0025
I_{max}	81873	17940	69838
Number of points	14121	14374	13376
Refinement			
Refinement		Rietveld	
Background function		Legendre polynomials, 15 terms	
Number of reflections (all/observed)	1920/1215	1930/839	2739/2321
Among them			
Main (all/observed)	645/464	647/348	548/493
1st order satellites (all/observed)	1275/751	1283/491	1099/935
2nd order satellites (all/observed)	–	–	1092/893
No. of refined parameters/ refined atomic parameters	55/31	55/27	75/47
R and R_w (%) for Bragg reflections (R_{all}/R_{obs})	5.89/3.91 and 2.41/2.32	6.19/3.40 and 2.76/2.48	4.76/4.00 and 2.41/2.37
Among them:			
Main	2.93/2.36 and 1.85/1.81	3.36/2.42 and 2.09/1.92	2.33/2.09 and 1.57/1.55
1st order satellites	10.27/7.03 and 3.87/3.66	10.86/6.51 and 4.63/4.08	6.73/5.84 and 3.42/3.37
2nd order satellites	–	–	8.81/7.07 and 2.99/2.93
R factors and goodness of fit	R_p = 0.0736, R_{wp} = 0.0957, R_{exp} = 0.0709, $R(F)$ = 0.0589, χ^2 = 1.35	R_p = 0.1097, R_{wp} = 0.1461, R_{exp} = 0.1485, $R(F)$ = 0.0610, χ^2 = 0.98	R_p = 0.0661, R_{wp} = 0.0922, R_{exp} = 0.0654, $R(F)$ = 0.0476, χ^2 = 1.41
Max./min. residual density (e Å^{-3})	2.77/−4.7	2.35/−4.99	2.62/−3.01
CSD number	2500363	2500364	2500362

Computer programs: *JANA2000* (Petříček *et al.*, 2014).

incommensurately modulated $M_{1/8}Pr_{5/8}\square_{1/4}MoO_4$ (M = Li, Na, K) structures was performed using the *JANA2006* software (Petříček *et al.*, 2014). Illustrations were produced with this package in combination with the program *DIAMOND* (Brandenburg, 1999).

3. Results

3.1. Elemental composition

^{39}K and ^{141}Pr isotopes were used for ICP-MS measurements to determine the K:Pr ratio for the bulk $K_{1/8}Pr_{5/8}\square_{1/4}MoO_4$ sample. Measurements using different isotopes yielded identical results with no overlaps. The reproducibility (s_r) of the ICP-MS results was 0.1 for both K and Pr determination. Apparently, the high value of s_r is associated with the interfering effect of argon plasma $^{38}Ar+^{40}Ar^+$ on the determination of ^{39}K and ^{40}K isotopes, as well as with the possible overlap of polyatomic ions with ^{141}Pr isotope. The formation of polyatomic ions in plasma is probabilistic in nature, so it is difficult to take them into account in a control experiment. Pr (417.939 nm) and K (766.490 nm) lines were used for ICP-OES measurements. This method reduced the s_r of Pr and K determination to 0.05. The time of TXRF spectrum acquisition was 250 s (lifetime). To verify substrate purity, admixtures were determined after cleaning the substrate with HNO_3 solution (10%). A Ga^{3+} ion solution with the concentration 50 mg l^{-1} as an internal standard was used for quantitative calculations.

SEM-EDX analysis revealed K:Pr:Mo ratios in $K_{1/8}Pr_{5/8}MoO_4$ of 0.12:0.61:1 (7.13 ± 0.26 at% K, 35.20 ± 0.67 at% Pr, 57.67 ± 0.87 at% Mo), which closely match the expected composition. Fig. S1 in supporting information shows representative TXRF and SEM-EDX spectra for the $K_{1/8}Pr_{5/8}MoO_4$ sample. Table 2 summarizes the K:Pr ratio results in $K_{1/8}Pr_{5/8}MoO_4$ determined by different methods. The determined K:Pr ratio is consistent with expected values.

Table 2
K:Pr ratio in $K_{1/8}Pr_{5/8}\square_{1/4}MoO_4$ determined by ICP-MS, ICP-OES, TXRF and SEM-EDX.

Compound	ICP-MS	ICP-OES	TXRF	SEM-EDX
$K_{1/8}Pr_{5/8}\square_{1/4}MoO_4$	1:5.2 ± 0.2	1:5.0 ± 0.3	1:4.8 ± 0.3	1:4.9 ± 0.3

3.2. Preliminary characterization

Fig. 1 shows parts of powder X-ray diffraction patterns of $M_{1/8}Pr_{5/8}\square_{1/4}MoO_4$ (M = Ag, Li, Na, K) phases. Similar to $Ag_{1/8}Pr_{5/8}MoO_4$ (Morozov *et al.*, 2006), the PXRD patterns of $M_{1/8}Pr_{5/8}\square_{1/4}MoO_4$ (M = Li, Na, K) contain intense reflections corresponding to the scheelite-type structure and weaker satellite reflections. Earlier the appearance of weaker reflections was observed on PXRD patterns of $Na_{1/8}Pr_{5/8}\square_{1/4}MoO_4$ (Dhanya *et al.*, 2019). The unit-cell parameters were determined by Le Bail decomposition (Le Bail *et al.*, 1988) in $I2/b(\alpha\beta0)00$ superspace group using *JANA2006* software (Petříček *et al.*, 2014).

3.3. Refinement of $M_{1/8}Pr_{5/8}\square_{1/4}MoO_4$ (M = Li, Na, K) crystal structures

Synchrotron powder X-ray diffraction (SXRD) data was used to refine crystal structures of the $M_{1/8}Pr_{5/8}\square_{1/4}MoO_4$ (M = Li, Na, K) phases. The incommensurately modulated structures were refined from powder diffraction intensities using superspace group $I2/b(\alpha\beta0)00$. Fig. 2 shows the observed electron density along the internal axis, x_4, calculated in the vicinity of A position for the $M_{1/8}Pr_{5/8}MoO_4$ [M = Li (*a*), Na (*b*), K (*c*)] structures. The continuous variation of the electron density distribution along the x_4 axis indicates the wavy behavior of the A position occupation by M/Pr and vacancies. Based on refined structures of other scheelite-related compounds (Abakumov *et al.*, 2014; Arakcheeva *et al.*, 2012; Batuk *et al.*, 2017; Morozov *et al.*, 2013; Morozov *et al.*, 2017; Morozov *et al.*, 2018; Morozov *et al.*, 2023), we tested different models during the Rietveld refinement. Appendix 1 of the supporting information provides detailed descriptions of the models. The nine models (i)–(ix) differ by the function used for the occupancy of the A position and by the function used for the displacive modulation. We constrained all A site cations to the same coordinates, displacive modulation functions, and isotropic atomic displacement parameters (ADPs), and refined x_4^0 coordinates (except x_4^0 = 0 and x_4^0 = 0.5) and lengths (δ) of the atomic domains. Tables S1–S3 and Figs. S2 and S3 list results of the Rietveld refinement of the structures in these models.

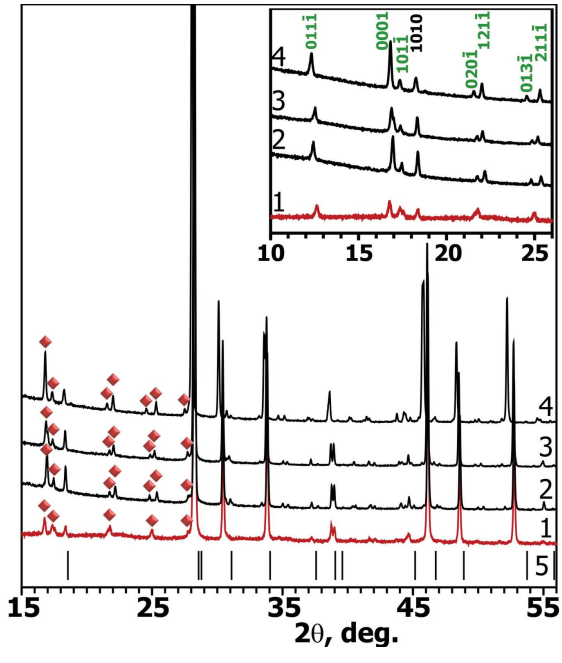

Figure 1
Parts of PXRD patterns of $M_{1/8}Pr_{5/8}MoO_4$ [M = Ag (1) (Morozov *et al.*, 2006*b*), Li (2), Na (3), K (4)] phases. Bragg reflections (5) for $CaMoO_4$ (JCPDS, PDF2 51-0267) are shown. The satellite reflections are indicated with red diamonds. Inset shows low-angle parts of the profile. The indexation of some satellite (green) and main (black) reflections are shown.

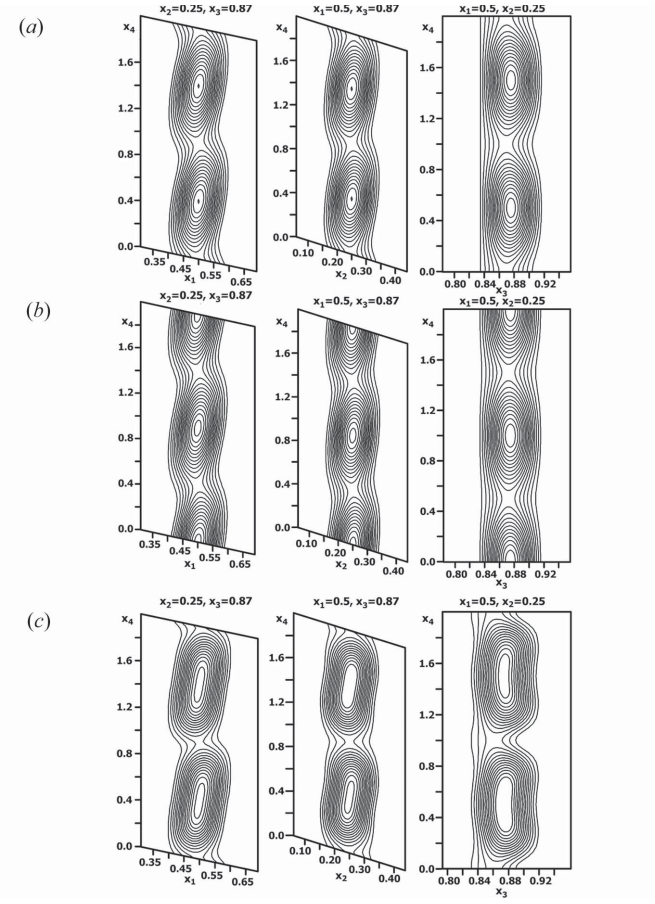

Figure 2
The vicinity of the A position in the structural model for the $M_{1/8}Pr_{5/8}MoO_4$ [M = Li (*a*), Na (*b*), K (*c*)] structures. The x_1x_4, x_2x_4, and x_3x_4 sections are presented for observed electron density maps. Lines show positive values of the electron density. The step between lines is 10 Å^{-3} for electron density.

3.3.1. $M_{1/8}Pr_{5/8}\square_{1/4}MoO_4$ (M = Li, Na) structures

Comparing the refinement results of all models with one [crenel-1H (ii), crenel-1L (iii)], crenel-3H (vi), crenel-3L (vii), crenel-4H (viii), and crenel-4L (ix)] and three crenel domains of Pr [crenel-2H (iv) and crenel-2L (v)] shows that the first model (i) has better reliability factors for all reflections (Tables S1 and S2). The harmonic model (i) demonstrates the best agreement with experimental data (Figs. S2 and S3). It also shows the best reliability factors for main [R_F(main reflections) = 2.93% (Li) and 3.72% (Na)] and for the first-order satellites [R_F(first-order satellites) = 10.27% (Li) and 11.79% (Na)] (Tables S1 and S2). The bond valence sums (BVS) variations for M and Pr in $M_{1/8}Pr_{5/8}MoO_4$ (M = Li, Na) structures for refinement models with the best reliability factors for all reflections are shown in Figs. S4 and S5. BVS were calculated with 3 Å cutoff. BVS for Li differ only slightly among the three refinement models, with ranges 0.71–0.95 for (i), 0.82–0.88 for (iv) and 0.83–0.91 for (v). The difference in BVS for Pr in $Li_{1/8}Pr_{5/8}MoO_4$ structure is greater for these models, but not wrong: ranges are 2.05–3.24 for model (i), 2.92–3.30 (Pr1) and 2.28–2.55 (Pr2) for (iv), 3.06–3.41 (Pr1) and 2.30–2.68 (Pr2) for (v). Consequently, selecting a refinement model for the $Li_{1/8}Pr_{5/8}MoO_4$ structure based solely on BVS variations for Li and Pr is challenging.

A similar situation was observed when choosing between refinement models for the $Na_{1/8}Pr_{5/8}MoO_4$ structure based on BVS variations for Na and Pr. Only the crenel-4H (viii) model model can be clearly rejected, as it yields erroneous BVS ranges of 1.83–4.08 for Pr and 1.58–1.63 for Na. In $Li_{1/8}Pr_{5/8}MoO_4$, BVSs differ slightly between the three models, ranging from 2.13 to 3.17 for (i), 2.94 to 3.33 (Pr1) and 2.20 to 2.55 (Pr2) for (iv), 3.12 to 3.45 (Pr1) and 2.24 to 2.65 (Pr2) for (v). The BVS values for Na in these models show a wider spread than those for Li in the $Li_{1/8}Pr_{5/8}MoO_4$, with ranges 0.95–1.29 for model (i); 1.11–1.21 for (iv), and 1.12–1.24 for (v).

The t-plots of BVS variations for K and Pr cations in $K_{1/8}Pr_{5/8}\square_{1/4}MoO_4$ structure, calculated using the harmonic model, are incorrect. In contrast, the t-plots for K and Pr cations are similar for the crenel-2H (iv) and crenel-2L (v) models. The harmonic model for $M_{1/8}Pr_{5/8}\square_{1/4}MoO_4$ (M = Li, Na) structures fits the experimental data significantly better than all crenel models. Therefore, model (i) with the harmo-

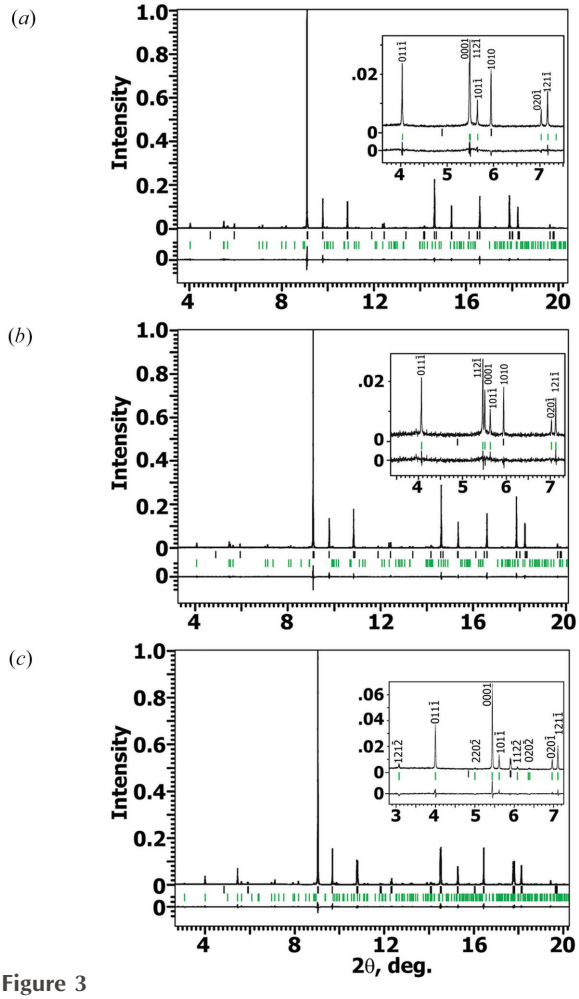

Figure 3
Experimental, calculated and difference SXPD profiles after Rietveld refinement of $M_{1/8}Pr_{5/8}MoO_4$ [M = Li (*a*), Na (*b*), K (*c*)]. Insets show a low-angle part of the profile. Black and green bars mark the positions of the main and satellite reflections, respectively.

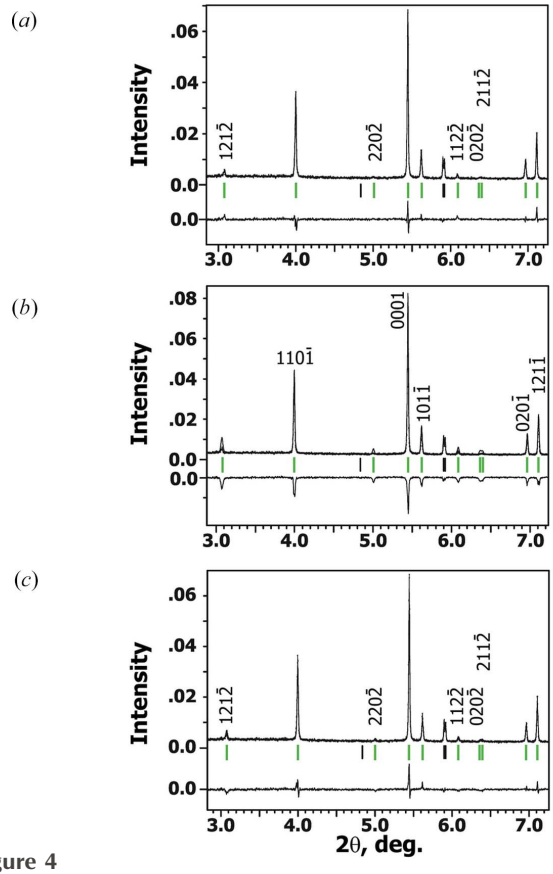

Figure 4
Illustration of the different model refinements performed from SXPD data for $K_{0.145}Pr_{0.618}\square_{0.237}MoO_4$: (*a*) wave occupation function approximation (harmonic model); (*b*) crenel-1H approximation; (*c*) crenel-2H approximation. The lower-angle parts of the experimental, calculated and difference SXPD profiles with the indexation of reflections are shown. Black and green bars mark the positions of the main and satellite reflections, respectively.

nically occupational modulation of the *A* site was adopted for $M_{1/8}Pr_{5/8}MoO_4$ (*M* = Li, Na) structure refinements.

The harmonic model assumes that the occupancy factor of the *A* site is harmonically modulated and there is no ordering between different *A* cations and vacancies. Three species with different scattering factors (Pr, *M* and vacancy) occupy the same crystallographic position. Therefore, their influence on the overall modulation of the scattering density at this position cannot be determined unambiguously. Only an antiphase occupancy modulation of the *M* and Pr atoms agrees with the experimentally determined modulation of the scattering density at the *A* position.

No satellites with an order higher than one were observed on the SXPD pattern of $M_{1/8}Pr_{5/8}\square_{1/4}MoO_4$ (*M* = Li, Na); therefore, the displacive modulations were fitted with a first-order harmonic. Parameters of the modulation functions that did not exceed their standard deviations were fixed to 0 in the refinement. Identical atomic coordinates and ADPs were refined for the *M* and Pr atoms. O atoms were refined with common ADPs. Table 1 lists the crystallographic information; Tables S4 and S5 list the atomic parameters and the coefficients of the modulation functions; Tables S6 and S7 give the main interatomic distances. Fig. 3 shows the experimental, calculated, and difference SXPD profiles of the $M_{1/8}Pr_{5/8}\square_{1/4}MoO_4$ [*M* = Li (*a*), Na (*b*)] phases after the Rietveld refinement.

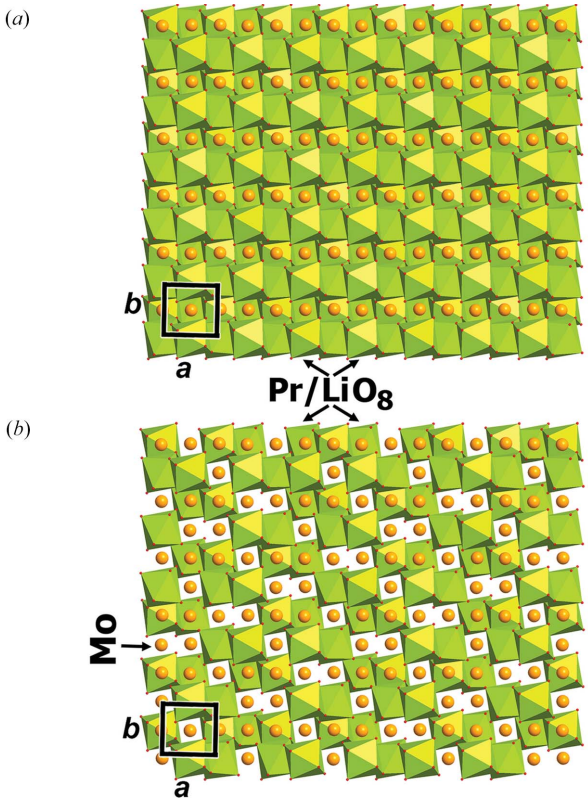

Figure 5
Overview of the $Li_{1/8}Pr_{5/8}\square_{1/4}MoO_4$ O ($7a \times 6b \times 1c$ supercell) with the occupation of the *A* sites ($A = Pr_{1-x}Li_x$) (*a*) > 5% and (*b*) > 50%. Pr/LiO_8 polyhedra are shown as green colour. The Mo and O atoms are shown as yellow and red spheres, respectively.

3.3.2. $K_{1/8}Pr_{5/8}MoO_4$ structure

In contrast to the PXRD patterns of $M_{1/8}Pr_{5/8}\square_{1/4}MoO_4$ (*M* = Ag, Li, Na, K) (Fig. 1) and the SXPD patterns of $M_{1/8}Pr_{5/8}\square_{1/4}MoO_4$ [*M* = Li, Na (Fig. 3(*a*), 3(*b*)], second-order satellites appear on the SXPD patterns of $K_{1/8}Pr_{5/8}\square_{1/4}MoO_4$ [Figs. 3(*c*) and 4]. The refinement of the $K_{1/8}Pr_{5/8}\square_{1/4}MoO_4$ structure in harmonic model (i) showed poor agreement between the calculated and experimental profiles (Table S3). Therefore, we discarded model (i).

Comparing the refinement results of all models shows that model (iv) has better reliability factors for all reflections with one [crenel-1H (ii), crenel-1L (iii), crenel-3H (vi), crenel-3L (vii), crenel-4H (viii), and crenel-4L (ix)]. Three crenel domains of Pr [crenel-2H (iv) and crenel-2L (v)] have better reliability factors for all reflections (Table S3). The model (iv) demonstrates the best agreement with the experimental data (Fig. 4) and best reliability factors for main reflections [R_F(main reflections) = 2.33% and for the first- and second-order satellites R_F(first-order satellites) = 6.73% and R_F(second-order satellites) = 8.81%] (Table S3). The bond valence sums variations in $K_{1/8}Pr_{5/8}\square_{1/4}MoO_4$ structure for refinement models with the best reliability factors for all reflections are shown in Fig. S6. The model with the displacive modulation fitted with harmonic functions with the second-order Fourier amplitudes for atom positions for $K_{1/8}Pr_{5/8}\square_{1/4}MoO_4$ structure (Appendix 1 of the supporting information) fits the experimental data significantly better than the harmonic model and other crenel models.

Therefore, model (iv) with the step-like occupational modulation and three crenel domains of Pr was adopted. The displacive modulations were fitted with a second-order harmonic.

Refining the coordinates and lengths of three atomic domains results in the composition $K_{0.145}Pr_{0.618}\square_{0.237}MoO_4$. The reliability factors show good agreement between the calculated and experimental profiles (Table 1). Fig. 3(*c*) shows the experimental, calculated, and difference SXPD profiles of the $K_{0.145}Pr_{0.618}\square_{0.237}MoO_4$ phases after the Rietveld refinement. Table S8 lists the atomic parameters and the coefficients of the modulation functions; Table S9 gives the main interatomic distances.

4. Discussion

Overview images of the $Li_{1/8}Pr_{5/8}\square_{1/4}MoO_4$ structure with the occupation of the *A*-sites ($A = Pr_{1-x}Li_x$) > 5% and > 50% are shown in Fig. 5. The scheelite-type ABO_4 ($CaWO_4$) structure consists of a 3D framework. Along the *c* axis, it contains columns of vertex sharing AO_8 polyhedra and BO_4 tetrahedra. The scheelite-type structure can accommodate a high number of vacancies at the *A*-cation position, leading to a cation ratio where $(A'+A'') < (B'+B'')$, *i.e.* $n < m$. The *A*-site cation ordering can occur in scheelites with or without *A*-site cation vacancies (Morozov *et al.*, 2006*a*; Morozov *et al.*, 2015). The *A* cations and vacancies can order, frequently forming incommensurately modulated structures (Abakumov *et al.*, 2014;

Arakcheeva *et al.*, 2012; Batuk *et al.*, 2017; Morozov *et al.*, 2013; Morozov *et al.*, 2017; Morozov *et al.*, 2018; Morozov *et al.*, 2023). It was suspected that the main driving force for the compositional modulation was a tendency to optimize the bond valence balance for the *A* cations and oxygen atoms (Abakumov *et al.*, 2014).

Earlier, we studied the structure and the luminescence properties of Eu-based cation deficient scheelite-related phases (Arakcheeva *et al.*, 2012; Batuk *et al.*, 2017; Morozov *et al.*, 2013; Morozov *et al.*, 2017; Morozov *et al.*, 2023). In these Eu-based scheelite-related incommensurately modulated structures, Eu-aggregates exist in two forms: $[Eu_2O_{14}]$ dimers and infinite chains of EuO_8 polyhedra parallel to the *c* axis (Arakcheeva *et al.*, 2012; Morozov *et al.*, 2017). A correlation was proposed between the relative amount of $[Eu^{3+}{}_2O_{14}]$ dimers and the characteristic parameters of Eu^{3+}-centered luminescence of the $Na_xEu^{3+}{}_{(2-x)/3}\square_{(1-x)/3}MoO_4$ (Arakcheeva *et al.*, 2012) and $Ag_xEu_{(2-x)/3}\square_{(1-2x)/3}WO_4$ (Morozov *et al.*, 2017) phases. Luminescence parameters increase with the growing relative amount of Eu^{3+} dimers.

Figs. 6 and 7 show the main structural parameters of the $M_{1/8}Pr_{5/8}\square_{1/4}MoO_4$ (*M* = Li, Na) as *t*-plots, providing a comprehensive overview of the parameters variation in different unit cells of the basic structure. The occupancy modulation waves for the Li/Na and Pr atoms demonstrate an antiphase relation, peaking at $t = 1/2$ and $t = 0$, respectively. However, the maximum Pr content for the *A* site is observed at $t = 0$ in $Li_{1/8}Pr_{5/8}\square_{1/4}MoO_4$ [$A = 0.94Pr^{3+} + 0.06Li^+$, Fig. 6(*a*)] and at $t = 1/2$ in $Na_{1/8}Pr_{5/8}\square_{1/4}MoO_4$ structure [$A = 0.94Pr^{3+} + 0.06Na^+$, Fig. 7(*a*)]. According to the SXPD data, there is no ordering between the Li^+/Na^+ and Pr^{3+} cations. This agrees with the published criterion (Abakumov *et al.*, 2014) that cation ordering requires an ionic size difference of ~0.35 Å [in the case of $M_{1/8}Pr_{5/8}\square_{1/4}MoO_4$: $\Delta r \sim 0.206$ Å (Li) and $\Delta r \sim 0.054$ Å (Na); r(Pr) = 1.126 Å, r(Na) = 1.18 Å, r(Li) = 0.92 Å, CN = 8 (Shannon, 1976)].

The distortion of the PrO_8 and MO_8 polyhedra is practically independent of the *M* radius. The Pr/*M*–O interatomic distances in the AO_8 polyhedra vary between 2.372–2.619 Å and 2.405–2.635 Å [Figs. 6(*b*), 7(*b*) and Tables S6–S7] for Li and Na, respectively. Notably, all eight Pr/*M*–O distances change almost synchronously, indicating 'breathing' of the PrO_8 and MO_8 polyhedra, and not the displacement of the Pr/*M* cation from the center.

Compared to $M_{1/8}Pr_{5/8}\square_{1/4}MoO_4$ (*M* = Li, Na), the K^+ and Pr^{3+} cations are ordered in the $K_{0.145}Pr_{0.618}\square_{0.237}MoO_4$ structure. This ordering occurs because the ionic size difference of $\Delta r = 0.384$ Å [r(Pr) = 1.126 Å, r(K) = 1.51 Å, CN = 8 (Shannon, 1976)] satisfies the cation ordering criterion (Abakumov *et al.*, 2014). In the $K_{0.145}Pr_{0.618}\square_{0.237}MoO_4$ scheelite-type structure, columns of [...–(PrO_8/KO_8)–MoO_4–...] and [...–□–MoO_4–...] run along the *c* axis [Fig. 8(*a*)]. Basically, the framework can be considered as consisting of groups of AO_8 polyhedra alternating with cation vacancies. An *A*-cationic subset of the $K_{0.145}Pr_{0.618}\square_{0.237}MoO_4$ aperiodic structure is shown in Fig. 8(*b*). In contrast to the $Na_xEu^{3+}{}_{(2-x)/3}\square_{(1-2x/3}MoO_4$ (Arakcheeva *et al.*, 2012; Batuk *et al.*, 2017; Morozov *et al.*, 2017; Morozov *et al.*, 2018) and $Ag_xR_{(2-x)/3}\square_{(1-2x)/3}WO_4$ (*R* = Eu, Sm), only extended $[PrO_8]_n$

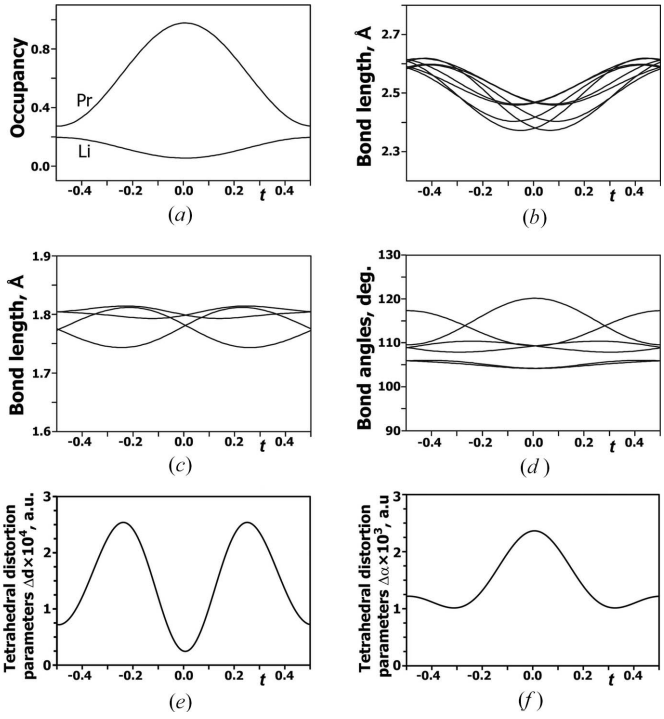

Figure 6
t-plots in the $Li_{1/8}Pr_{5/8}\square_{1/4}MoO_4$ structure: variation of the Li/Pr occupancies (*a*), *A*—O bond length (*b*), Mo—O bond length (*c*), O—Mo—O bond angles (*d*) and tetrahedral distortion parameters Δd (*e*) and $\Delta\alpha$ (*f*).

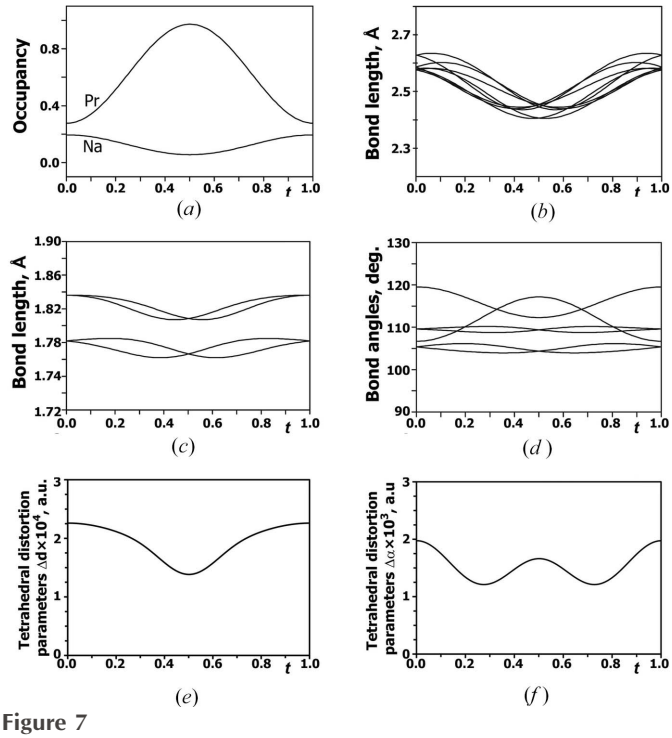

Figure 7
t-plots in the $Na_{1/8}Pr_{5/8}\square_{1/4}MoO_4$ structure: variation of the Na/Pr occupancies (*a*); *A*—O bond length (*b*); Mo—O bond length (*c*); O—Mo—O bond angles (*d*); and tetrahedral distortion parameters $d\Delta$ (*e*) and $\Delta\alpha$ (*f*).

chains exist in the $K_{0.145}Pr_{0.618}\square_{0.237}MoO_4$ structure. Two types of K fragments can be distinguished in the structure: single KO_8 polyhedra and $[K_2O_{14}]$ dimers with K–K distances of 3.94 Å within the dimers and 5.18 Å between them [Fig. 9(*a*)]. Neighboring K fragments are separated by vacancies [Fig. 8(*b*)].

Fig. 9(*b*) shows one layer of the incommensurately modulated $K_{0.145}Pr_{0.618}\square_{0.237}MoO_4$ structure and of the subset of the *A*-cations in the [001] projection. The cation order is defined by the coefficients α and β of the modulation vector $\mathbf{q} = \alpha\mathbf{a}^* + \beta\mathbf{b}^*$ (Table 1) and the parameters of three atomic domains for the same cation position (Pr1, Pr2 and K) (Table S8). As can be deduced from Fig. 9(*b*), the ordering of Pr/K cations and vacancies in the *A* position is periodic along the *c* axis but aperiodic (modulated) in the *ab* plane.

Fig. 10 shows a variation of the K/Pr occupancies, Pr/K—O bond lengths, and Pr–Pr distances for the $K_{0.145}Pr_{0.618}\square_{0.237}MoO_4$ structure. The PrO_8 and KO_8 polyhedra are significantly distorted. The Pr—O bond distances are higher for Pr2 (2.441–2.800 Å) than for Pr1 (2.310–2.600 Å), while the K–O distances vary between 2.367 and 2.685 Å [Fig. 10(*b*)]. The Pr–Pr distances within the $[PrO_8]_n$ chains range from 3.759 to 4.147 Å [Fig. 9(*c*), Table S9].

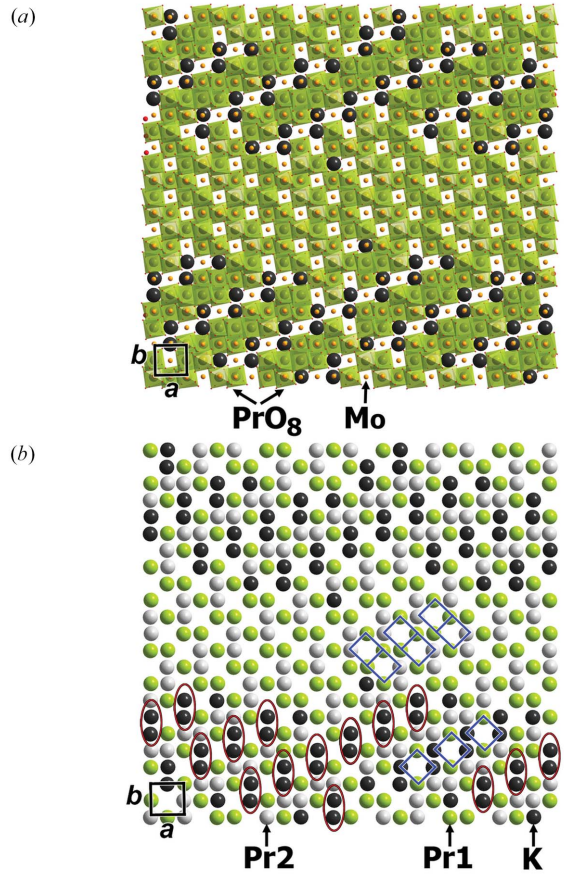

Figure 8
(*a*) Overview of the $12a \times 11b \times 1c$ supercell in the *ab* projection (*a*) and *A*-cation subset (*b*) of the $K_{0.145}Pr_{0.618}\square_{0.237}MoO_4$ aperiodic structure. PrO_8 polyhedra are shown in green. K, Mo and O atoms are shown as black, yellow and red spheres, respectively. Blue squares indicate some of the vacancies in the structure. $[K_2O_{14}]$ dimers are marked by red ellipses.

The Mo—O bond lengths and O—Mo—O bond angles in *t*-plots for the $K_{0.145}Pr_{0.618}\square_{0.237}MoO_4$ structure are shown in Figs. 11(*a*) and 11(*b*), respectively. The MoO_4 tetrahedra exhibit minimal distortion, with Mo–O distances remaining nearly independent of the *M* radius. These distances range from 1.739 to 1.832 Å (Table S9) for $K_{0.145}Pr_{0.618}\square_{0.237}MoO_4$ [*r*(K) = 1.51 Å, CN = 8], 1.762–1.836 Å (Table S7) for $Na_{1/8}Pr_{5/8}\square_{1/4}MoO_4$ [*r*(Na) = 1.18 Å, CN = 8] and 1.744–1.814 Å (Table S6) for $Li_{1/8}Pr_{5/8}\square_{1/4}MoO_4$ [*r*(Li) = 0.92 Å, CN = 8] (Shannon, 1976).

The O—Mo—O bond angles in $M_{1/8}Pr_{5/8}\square_{1/4}MoO_4$ (*M* = Li, Na, K) (Figs. 6–7 and Fig. 11) deviate significantly from the ideal tetrahedral angle of 109.5° varying in the range from 100.3 (8) to 124.5 (8)° for $K_{0.145}Pr_{0.618}\square_{0.237}MoO_4$ [*r*(K) = 1.51 Å, CN = 8], 104.0 (7)–119.5 (8)° for $Na_{1/8}Pr_{5/8}\square_{1/4}MoO_4$ [*r*(Na) = 1.18 Å, CN = 8], and 104.7 (4)–118.7 (5)° for $Li_{1/8}Pr_{5/8}\square_{1/4}MoO_4$ [*r*(Li) = 0.92 Å, CN = 8] (Shannon, 1976).

Usually the structure adopts changing size and charge of the cations at the *A* position through the deformation of the MoO_4 tetrahedra, which occurs as an antiphase alternation of two distortion modes: stretching the Mo—O bonds or bending the O—Mo—O bond angles. The tetrahedral distortion parameters Δd and $\Delta\alpha$, characterizing the deviations of the Mo—O interatomic distances from the average value and the deviations of the O—Mo—O bond angles from the ideal tetrahedral angle were used for analysis of the distortion of

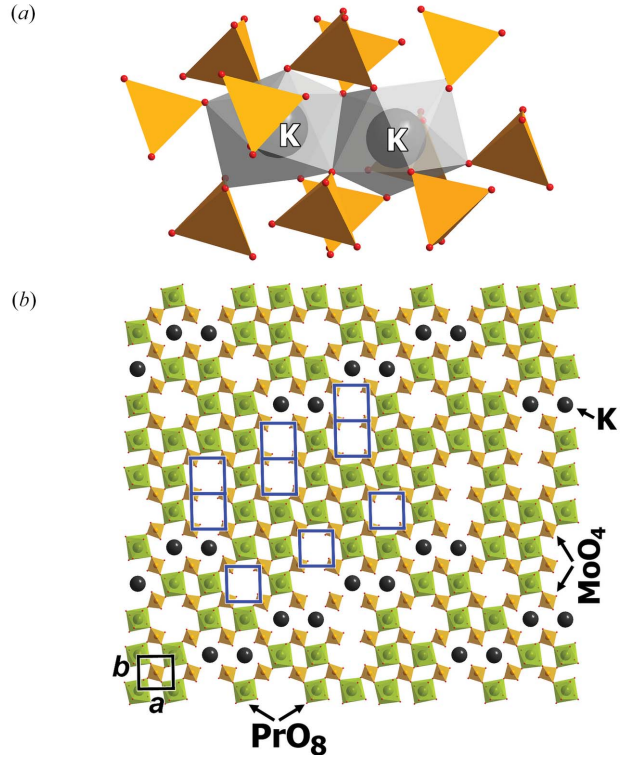

Figure 9
(*a*) A single $[K_2O_{14}]$ dimer surrounded by MoO_4 tetrahedra; (*b*) one layer (along *z*, $0.40 \leq z \leq 0.85$) of the $12a \times 11b$ supercell of $K_{0.145}Pr_{0.618}\square_{0.237}MoO_4$. Blue squares indicate some of the vacancies in the structure.

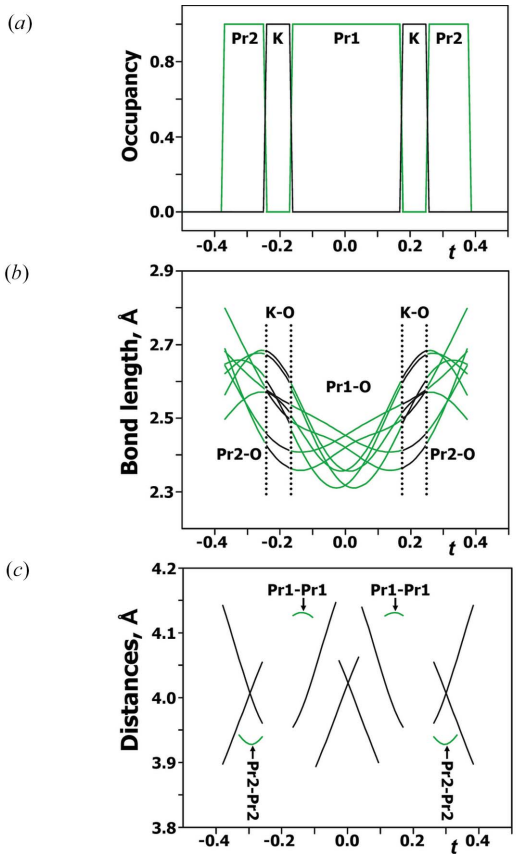

Figure 10
t-plots for the $K_{0.145}Pr_{0.618}\square_{0.237}MoO_4$ structure: (*a*) variation of the K/Pr occupancies, (*b*) *A*—O bond lengths and (*c*) Pr–Pr distances. Black lines show Pr1–Pr2 distances. Green lines show Pr1–Pr1 and Pr2–Pr2 distances.

the MoO_4 in $M_{1/8}Pr_{5/8}\square_{1/4}MoO_4$ (*M* = Li, Na, K) (Figs. 6, 7 and 11). The parameters are defined as

$$\Delta d = 1/4 \sum_{n=1\text{-}4} \left[(d_n - d)/d\right]^2, \Delta\alpha = 1/6 \sum_{n=1\text{-}6} \left[(\alpha_n - \alpha)/\alpha\right]^2,$$

where d_n is the individual Mo—O bond length, d is the average Mo—O bond length, α_n is the individual O—Mo—O bond angle and α is the ideal tetrahedral angle.

The occupancy coefficients of the Li/Na and Pr positions are modulated in antiphase [Figs. 6(*a*) and 7(*a*)]. The *A*–O distances vary significantly, being smallest and largest at the unit cells with the highest and lowest occupancy of the Pr positions, respectively [Figs. 6(*b*) and 7(*b*)]. At the same time, the occupancy of the *A* site with the Pr^{3+} cations in $K_{0.145}Pr_{0.618}\square_{0.237}MoO_4$ causes significant contraction of the *A*–O distance [Fig. 10(*b*)]. This tendency agrees with the smaller ionic radius of the Pr^{3+} cations (r = 1.126 Å, CN = 8) compared to that of K (r = 1.51 Å, CN = 8) (Shannon, 1976).

The stretching distortion of the Mo—O bonds (Δd) and distortion of the O—Mo—O angles ($\Delta\alpha$) depend on the difference between the ionic radii of the *M* and Pr cations ($\Delta r = |r(M)–r(A'')|$). The Δd and $\Delta\alpha$ parameters rise with increasing of Δr: Δd = 1.8–2.6 × 10^{-4} and $\Delta\alpha$ = 1.2–2.0 × 10^{-3} for $Na_{1/8}Pr_{5/8}\square_{1/4}MoO_4$ (Δr = 0.054 Å); Δd = 0.2–2.5 × 10^{-4} and $\Delta\alpha$ = 1.0–2.4 × 10^{-3} for $Li_{1/8}Pr_{5/8}\square_{1/4}MoO_4$ (Δr = 0.206 Å), and Δd = 0–4.8 × 10^{-4} and $\Delta\alpha$ = 1.5–4.0 × 10^{-3} for $K_{0.145}Pr_{0.618}\square_{0.237}MoO_4$ (Δr = 0.384 Å) (Shannon, 1976). The smallest stretching distortion of the Mo—O bonds (minimal values of Δd) occurs in the unit cells with the highest Pr content [Figs. 6(*e*) and 7(*e*)] in $M_{1/8}Pr_{5/8}MoO_4$ (*M* = Li, Na) while the largest bending distortion of the O—Mo—O angles (largest $\Delta\alpha$) occurs in the unit cells with the highest Pr content for *M* = Li and the lowest Pr content for *M* = Na [Figs. 6(*f*) and 7(*f*)]. The minimal values of Δd and the largest $\Delta\alpha$ are observed for t = 1/2 (center of Pr1 crenel domain) while the maximal Δd and smallest $\Delta\alpha$ are found for t = ∼0.323 and t = ∼0.677 (close to boundaries of Pr1 crenel domain) [Figs. 11(*c*) and 11(*d*)].

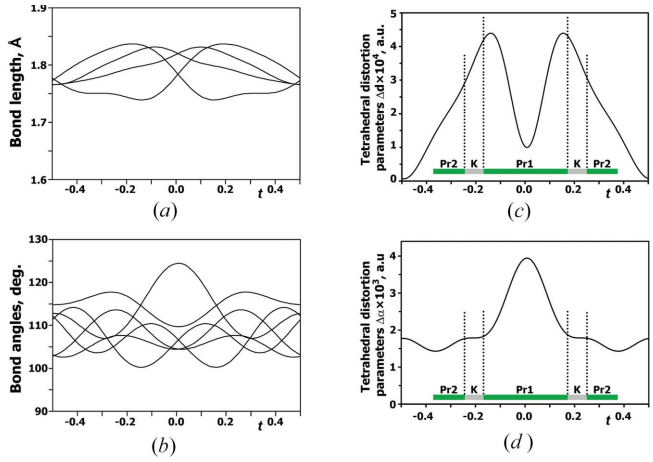

Figure 11
t-plots for the $K_{0.145}Pr_{0.618}\square_{0.237}MoO_4$ structure: Mo—O bond length (*a*); O—Mo—O bond angles (*b*), tetrahedral distortion parameters Δd (*c*) and $\Delta\alpha$ (*d*).

5. Conclusion

We investigated the effect of cationic composition on the ordering of the M^+/Pr^{3+} cations and vacancies for (3+1)D-modulated monoclinic $M_{1/8}Pr_{5/8}\square_{1/4}MoO_4$ (*M* = Li, Na, K) structures. The $M_{1/8}Pr_{5/8}\square_{1/4}MoO_4$ (*M* = Li, Na, K) structures were refined using synchrotron powder X-ray diffraction. $M_{1/8}Pr_{5/8}\square_{1/4}MoO_4$ (*M* = Li, Na, K) were synthesized using solid state reactions. Element contents were determined by different methods. Different models during the Rietveld refinement were tested based on earlier refined scheelite–related structures of other compounds. The cation ordering is not complete for $M_{1/8}Pr_{5/8}\square_{1/4}MoO_4$ (*M* = Li, Na, K) structures and better described with harmonic rather than with step–like occupational modulation functions. The occupancy modulation waves for the Li/Na and Pr atoms demonstrate an antiphase relation. In comparison with *M* = Li, Na the order of the K and Pr cations in the *A* position in $K_{1/8}Pr_{5/8}\square_{1/4}MoO_4$ structure is best approximated by crenel functions. Refining the coordinates and lengths of three atomic domains results in the composition $K_{0.145}Pr_{0.618}\square_{0.237}MoO_4$. In all cases the modulation arises from ordering of the *M*/Pr cations and the cation vacancies at the *A*-sublattice of the parent scheelite

ABO_4 structure. The distortion of the PrO_8 and MO_8 polyhedra is practically independent of the M radius. The refinements of the $M_{1/8}Pr_{5/8}\square_{1/4}MoO_4$ (M = Li, Na, K) structures reveal that the MoO_4^{2-} tetrahedra in scheelite-type compounds demonstrate a flexible geometry. Both Mo—O distances and O—Mo—O bond angles vary significantly with changing the population of the A site by cations with different cation size.

6. Supporting information

DTXRF and EDX spectra of $K_{1/8}Pr_{5/8}MoO_4$ (Fig. S1). Models tested during the Rietveld $Li_{1/8}Pr_{5/8}\square_{1/4}MoO_4$ refinement using the structure SXPD (Appendix 1). Characteristics of the different of the different model refinements model refinements performed of from PXPD data for $Li_{1/8}Pr_{5/8}\square_{1/4}MoO_4$ (Fig. S2). Characteristics of the different model refinements of $Na_{1/8}Pr_{5/8}\square_{1/4}MoO_4$ structure (Table S2). Illustration of the different model refinements performed from PXPD data for $Na_{1/8}Pr_{5/8}\square_{1/4}MoO_4$ (Fig. S3). *t*-plots of bond valence sums variations in $Li_{1/8}Pr_{5/8}\square 1/4MoO_4$ structure for refinement models with the best $Na_{1/8}Pr_{5/8}\square_{1/4}MoO_4$ reliability factors for all reflections (Fig. S4). *t*-plots of bond valence sums variations in $Na_{1/8}Pr_{5/8}\square_{1/4}MoO_4$ structure for refinement models with the best reliability factors for all reflections (Fig. S5). Characteristics of the different model refinements of $K_{1/8}Pr_{5/8}\square_{1/4}MoO_4$ structure (Table S3). *t*-plots of bond valence sums variations in $K_{1/8}Pr_{5/8}\square_{1/4}MoO_4$ structure for refinement models with the best reliability factors for all reflections (Fig. S6). Atomic coordinates, amplitudes of Fourier components for the occupational and displacive modulation functions and isotropic atomic displacement parameters for $Li_{1/8}Pr_{5/8}\square_{1/4}MoO_4$ structure (Table S4). Atomic coordinates, amplitudes of Fourier components for the occupational and displacive modulation functions and isotropic atomic displacement parameters for $Na_{1/8}Pr_{5/8}\square_{1/4}MoO_4$ structure (Table S5). Main interatomic distances for $Li_{1/8}Pr_{5/8}\square_{1/4}MoO_4$ (Table S6). Main interatomic distances for $Na_{1/8}Pr_{5/8}\square_{1/4}MoO_4$ (Table S7). Atomic coordinates, amplitudes of Fourier components for the occupational and displacive modulation functions and isotropic atomic displacement parameters for in $K_{0.145}Pr_{0.618}\square_{0.237}MoO_4$ structure (Table S8). Selected interatomic distances for $K_{0.145}P_{r0.618}\square_{0.237}MoO_4$. (Table S9).

Acknowledgements

The synthesis of samples was carried out within the framework of the state assignment of the BINM SB RAS. The synchrotron radiation experiments were conducted at the former NIMS beamline (BL15XU) of SPring-8 with the approval of the former NIMS Synchrotron X-ray Station. We thank Dr Y. Katsuya and Dr M. Tanaka for their help at SPring-8. The authors are grateful to A. M. Alekseeva (Chemistry Department, Moscow State University) for the SEM-EDX study.

Funding information

The following funding is acknowledged: State assignment "Substances and materials for ensuring safety, reliability and energy efficiency" (grant No. AAAA-A21-121011590086-0); state assignment of the BINM SB RAS; former NIMS Synchrotron X-ray Station (proposal No. 2019A4501).

References

Abakumov, A. M., Morozov, V. A., Tsirlin, A. A., Verbeeck, J. & Hadermann, J. (2014). *Inorg. Chem.* **53**, 9407–9415.
Arakcheeva, A., Logvinovich, D., Chapuis, G., Morozov, V., Eliseeva, S. V., Bünzli, J. G. & Pattison, P. (2012). *Chem. Sci.* **3**, 384–390.
Batuk, D., Batuk, M., Morozov, V. A., Meert, K. W., Smet, P. F., Poelman, D., Abakumov, A. M. & Hadermann, J. (2017). *J. Alloys Compd.* **706**, 358–369.
Bin, J., Liu, H., Mei, L., Liang, L., Gao, H., Li, H. & Liao, L. (2019). *Ceram. Int.* **45**, 1837–1845.
Brandenburg, K. (1999). *DIAMOND*, Version 2.1c. Crystal Impact GbR, Bonn, Germany.
Dhanya, J., Suresh, E. K., Naveenraj, R. & Ratheesh, R. (2019). *J. Elecron. Mater.* **48**, 4040–4049.
Huang, X., Lin, Z., Hu, Z., Zhang, L., Huang, J. & Wang, G. (2004). *J. Cryst. Growth* **269**, 401–407.
Huang, X., Li, B., Du, P., Guo, H., Cao, R., Yu, J. S., Wang, K. & Sun, X. W. (2018). *Dyes Pigments* **151**, 202–210.
Le Bail, A., Duroy, H. & Fourquet, J. L. (1988). *Mater. Res. Bull.* **23**, 447–452.
Logvinovich, D., Arakcheeva, A., Pattison, P., Eliseeva, S., Tomeš, P., Marozau, I. & Chapuis, G. (2010). *Inorg. Chem.* **49**, 1587–1594.
Lu, D., Gong, X., Chen, Y., Huang, J., Lin, Y., Luo, Z. & Huang, Y. (2018). *Opt. Mater. Expr.* **8**, 259.
Meert, K. W., Morozov, V. A., Abakumov, A. M., Hadermann, J., Poelman, D. & Smet, P. F. (2014). *Opt. Express* **22**, A961.
Morozov, V. A., Arakcheeva, A. V., Chapuis, G., Guiblin, N., Rossell, M. D. & Van Tendeloo, G. (2006*a*). *Chem. Mater.* **18**, 4075–4082.
Morozov, V. A., Arakcheeva, A. V., Pattison, P., Meert, K. W., Smet, P. F., Poelman, D., Gauquelin, N., Verbeeck, J., Abakumov, A. M. & Hadermann, J. (2015). *Chem. Mater.* **27**, 5519–5530.
Morozov, V., Arakcheeva, A., Redkin, B., Sinitsyn, V., Khasanov, S., Kudrenko, E., Raskina, M., Lebedev, O. & Van Tendeloo, G. (2012). *Inorg. Chem.* **51**, 5313–5324.
Morozov, V. A., Batuk, D., Batuk, M., Basovich, O. M., Khaikina, E. G., Deyneko, D. V., Lazoryak, B. I., Leonidov, I. I., Abakumov, A. M. & Hadermann, J. (2017). *Chem. Mater.* **29**, 8811–8823.
Morozov, V. A., Bertha, A., Meert, K. W., Van Rompaey, S., Batuk, D., Martinez, G. T., Van Aert, S., Smet, P. F., Raskina, M. V., Poelman, D., Abakumov, A. M. & Hadermann, J. (2013). *Chem. Mater.* **25**, 4387–4395.
Morozov, V. A., Mironov, A. V., Lazoryak, B. I., Khaikina, E. G., Basovich, O. M., Rossell, M. D. & Van Tendeloo, G. (2006*b*). *J. Solid State Chem.* **179**, 1183–1191.
Morozov, V., Deyneko, D., Basovich, O., Khaikina, E. G., Spassky, D., Morozov, A., Chernyshev, V., Abakumov, A. & Hadermann, J. (2018). *Chem. Mater.* **30**, 4788–4798.
Morozov, V. A., Lazoryak, B. I., Savina, A. A., Khaikina, E. G., Leonidov, I. I., Ishchenko, A. V. & Deyneko, D. V. (2023). *Materials* **16**, 4350.
Petříček, V., Dušek, M. & Palatinus, L. (2014). *Z. Kristallogr. Cryst. Mater.* **229**, 345–352.
Pusdekar, A., Ugemuge, N. S., Nafdey, R. & Moharil, S. V. (2025). *J. Mol. Struct.* **1319**, 139409.
Shannon, R. D. (1976). *Acta Cryst.* A**32**, 751–767.
Tanaka, M., Katsuya, Y. & Yamamoto, A. (2008). *Rev. Sci. Instrum.* **79**, 075106.

Tanaka, M., Katsuya, Y., Matsushita, Y. & Sakata, O. (2013). *J. Ceram. Soc. Japan* **121**, 287–290.
Singh, K., Pradhan, P., Priya, S., Mund, S. & Vaidyanathan, S. (2023). *Dalton Trans.* **52**, 13027–13057.
Wu, G., Zhang, Y., Kang, S., Yu, Z., Wang, X., Jin, D. & Wang, L. (2021). *Optik* **229**, 166271.
Zhang, C., Wang, Y., Wang, Z., Zhao, S., Lei, R. & Xu, S. (2024). *Ceram. Int.* **50**, 33225–33234.
Zhao, W., Zhou, W., Wei, B. & Wang, G. (2013). *Phys. Status Solidi A* **210**, 367–372.
Zhao, Y., Wang, X., Hu, R. & Li, Y. (2021). *Dalton Trans.* **50**, 15821–15830.